

Full paper

Structural and chemical synergistic effect of CoS nanoparticles and porous carbon nanorods for high-performance sodium storage



Limin Zhou^a, Kai Zhang^b, Jinzhi Sheng^a, Qinyou An^a, Zhanliang Tao^c, Yong-Mook Kang^b, Jun Chen^{c,*}, Liqiang Mai^{a,d,*}

^a State Key Laboratory of Advanced Technology for Materials Synthesis and Processing, Wuhan University of Technology, Hubei, Wuhan 430070, PR China

^b Department of Energy and Materials Engineering, Dongguk University-Seoul, Seoul 100-715, Republic of Korea

^c Key Laboratory of Advanced Energy Materials Chemistry (Ministry of Education), Collaborative Innovation Center of Chemical Science and Engineering, College of Chemistry, Nankai University, Tianjin 300071, PR China

^d Department of Chemistry, University of California, Berkeley, CA 94720, United States

ARTICLE INFO

Keywords:

Sodium-ion battery
Embedded structure
CoS
Anode material
High performance

ABSTRACT

Considering inherent large structural deterioration of conversion-type anode materials during repeated sodiation/desodiation process, the ingenious integration of both nanostructure engineering and chemical hybridization is highly desirable and challenging. Here, ultrafine CoS nanoparticles embedded in porous carbon nanorods (denoted as 7-CoS/C) were facilely fabricated via simultaneous in-situ carbonization and sulfidation of Co-metal organic frameworks (Co-MOF) and have been applied as anode materials for sodium-ion batteries (SIBs). Benefiting from the advantageous embedding architecture between the nanoparticles and porous nanorods, the 7-CoS/C delivers long-term cycling stability (542 mAh g⁻¹ after 2000 cycles with a capacity retention of 91.4% at 1 A g⁻¹) and excellent rate performance (discharge capacities of 510 mAh g⁻¹ at 5 A g⁻¹ and 356 mAh g⁻¹ even at 40 A g⁻¹), which is proved to be characterized of partial pseudocapacitive behaviors during the sodiation/desodiation process. In addition, Na₃V₂(PO₄)₃/7-CoS/C full cell with excessive amount of Na₃V₂(PO₄)₃ has been assembled and exhibits a capacity of 352 mAh g⁻¹ at 0.5 A g⁻¹. This meaningful approach can be extended to build embedded porous structure of other hybrid composites for next-generation energy-storage technology.

1. Introduction

In response to the environmental issues and increasing demands of available energy storage, sodium-ion batteries (SIBs) have recently captured a lot of interest as a reasonable substitution for lithium-ion batteries (LIBs) because of abundant sodium resources and low-cost sodium salts [1–7]. Anode materials, served as an important component of SIBs, are limited by low specific capacity and inadequate cyclability for sodium storage [8–11]. Harnessing transition-metal sulphides (TMSs) with conversion reactions is an effective strategy to solve the problem [8,12–16] due to the higher theoretical capacity compared to traditional intercalation materials such as graphite, NASICON-type NaTi₂(PO₄)₃, and TiS₂ [17–21]. Among various TMSs, CoS exhibits a theoretical capacity of 589 mAh g⁻¹ and is a promising available anode material, which has been successfully applied in LIBs [22,23]. However, the CoS electrode always suffers from serious pulverization problem caused by large structure change and the loss of electrical conductivity during the redox process similar

to other anode materials with conversion reaction, responsible for the large irreversible capacity, striking capacity fading, and poor rate performance [13,24].

Carbon-decorating is one common approach to improve reaction kinetics and cycling stability. Wang's group [25] synthesized a sandwich-like CoS/reduced graphene oxide (CoS/rGO) composite by hydrothermal method. When serving as the anode material for SIBs, it delivered a discharge capacity of 230.8 mAh g⁻¹ after 100 cycles at 0.1 A g⁻¹. At a high current density of 2 A g⁻¹, the capacity still reached 132.9 mAh g⁻¹. Peng et al. [26] used a solvothermal method to fabricate CoS nanoplates anchored on rGO. When applied as the anode for SIBs, high specific capacities of 636, 540, and 306 mAh g⁻¹ were achieved at 0.1, 1, and 10 A g⁻¹, respectively. Nevertheless, the introduction of extraneous conductive carbonaceous support may have difficulty in constructing hybrid with strong interaction force between metal sulphides and carbonaceous matrix to make the construct stability and integration [23].

Embedded structure with porous framework enables to efficiently

* Corresponding authors.

E-mail addresses: chenabc@nankai.edu.cn (J. Chen), mlq518@whut.edu.cn (L. Mai).

<http://dx.doi.org/10.1016/j.nanoen.2017.03.052>

Received 16 January 2017; Received in revised form 31 March 2017; Accepted 31 March 2017

Available online 02 April 2017

2211-2855/ © 2017 Elsevier Ltd. All rights reserved.

constrain the nanoparticles in given area. Sn nanoparticles embedded in nitrogen-doped porous carbon network fabricated by carbonizing Sn complex proves superior rate capability and stable cycle performance [27]. Besides, the acquisition of embedded architecture has been widely attempted through electrospinning technique and aerosol spray pyrolysis method to enhance the electrochemical property [28–32]. The two methods have been adopted to obtain Sn nanodots encapsulated in porous nitrogen-doped carbon nanofibers (Sn NDs@PNC nanofibers) [28] and ultrasmall Sn nanoparticles embedded in carbon [29], respectively. Both of them aimed at uniform distribution and nanosize of active Sn materials. In the case of promising CoS, Zhou's group [23] prepared 3D hollow CoS@porous carbon polyhedra/carbon nanotubes hybrids (CoS@PCP/CNTs) via using Co-based zeolitic imidazolate framework (ZIF-67) as the template. When evaluated as the anode for LIBs, it displayed high capacities of 1038, 979, 858, and 752 mAh g⁻¹ at current densities of 1, 2, 5, and 10 A g⁻¹, respectively. Lai's team [33] harnessed ZIF-67 derived carbon to confine CoS and Co₉S₈ hybrid, showing Na-storage capacities of 400, 340, 230 mAh g⁻¹ at 0.1, 0.5, 2 A g⁻¹, respectively. Yu's group [14] presented peapod-like carbon-encapsulated cobalt chalcogenide nanowires (CoS@carbon NWs), demonstrating 379 and 235 mAh g⁻¹ at current densities of 0.1 and 5 A g⁻¹, respectively. However, there is still a distance to reach a relatively high capacity at a high current density. To our best knowledge, the effective integrity between inherent merits and the design of external structure of materials is of great significance for the overall electrochemical performance [34–36]. Furthermore, except facilitating the accessibility of ions and electrons and buffering the volume fluctuation, embedded nano-structural hybridization protects the entire electrode from agglomeration and stripping and structural degradation [23,27,28], resulting in the maximized utilization to achieve high capacity and firm framework to realize long cycle life. Thus, the design of such nano-structural composite is worthy of being attempted.

Herein, we report the facile fabrication of ultrafine CoS nanoparticles (with an average size of ~7 nm) homogeneously embedded in porous N-doped carbon nanorods (denoted as 7-CoS/C) via simple heat treatment of the mixture of Co-metal organic frameworks (Co-MOF) and sublimed sulfur (Fig. 1a). Excitingly, the as-prepared 7-CoS/C exhibits long-term cycling stability of 542 mAh g⁻¹ after 2000 cycles at 1 A g⁻¹ between 0.6 and 3.0 V with a capacity retention of 91.4% (the capacity is calculated based on the whole mass of 7-CoS/C). In addition, the 7-CoS/C presents excellent rate performance, reflecting by the discharge capacities slightly change from 580 to 510 mAh g⁻¹ as current densities are gradually added from 0.5 to 5 A g⁻¹. Even at an ultrahigh current density of 40 A g⁻¹, the discharge capacity still reaches 356 mAh g⁻¹. The prominent performance is mainly attributed to the building of embedded porous architecture (Fig. 1b) as well as partial pseudocapacitive behaviors of the redox reactions and the usage of ether-based electrolyte. Furthermore, Na₃V₂(PO₄)₃/7-CoS/C full cell is assembled based on the excessive Na₃V₂(PO₄)₃, which delivers a reversible capacity of 352 mAh g⁻¹ at a current density of 0.5 A g⁻¹.

2. Results and discussion

The 7-CoS/C was prepared via directly heating Co-MOF and sublimed sulfur at 600 °C for 2 h. Co-MOF was synthesized by simple modified solvothermal method [37]. In brief, Co(NO₃)₂·6H₂O (3 mmol, 0.876 g), 1,3,5-benzenetricarboxylic acid (H₃BTC) (3 mmol, 0.633 g), and 4,4'-bipyridine (4,4'-bipy) (3 mmol, 0.576 g) as starting materials were added into 60 mL of dimethylformamide (DMF). After vigorous stirring for 30 min, the purple solution was transferred into a Teflon-lined stainless-steel autoclave and heated at 120 °C for 4 h. For comparison, 18.5-CoS/C was fabricated similar to the experimental procedure of 7-CoS/C, which only replaced the calcination temperature with 800 °C. Fig. 1c shows X-ray diffraction (XRD) patterns of the as-prepared 7-CoS/C and 18.5-CoS/C. All peaks are indexed to JCPDS No.

65-8977, indicating a hexagonal CoS with *P63/mmc* space group. In addition, the 7-CoS/C possesses broader half peak width than that of the 18.5-CoS/C, suggesting that the 7-CoS/C has smaller crystal size than that of the 18.5-CoS/C. Fig. 1d exhibits the corresponding crystal structure of CoS. There are two Co²⁺ ions and two S²⁻ ions in one crystal cell. Each Co²⁺ ion coordinates with six S²⁻ ions to form CoS₆ octahedron sharing edge and face. Fig. 1e-h present scanning electron microscopy (SEM), transmission electron microscopy (TEM) images and the particle size distribution diagram (the inset in Fig. 1g, by measuring 110 CoS nanoparticles using Nano-Measure software) of the 7-CoS/C, in which ultrafine CoS nanoparticles with an average size of 7 nm are uniformly embedded into porous carbon nanorods. The width and length of the nanorods are about 200 nm and 2 μm, respectively. Furthermore, the carbon content of the 7-CoS/C composite tested from the ANALYZER (CHNSO) is 14.6 wt%. This value is approximately consistent with the analytical result (14.1 wt%) determined from thermogravimetric analysis (TGA, Fig. S1). However, the particle size of 18.5-CoS/C is 18.5 nm (the inset in Fig. S1b) and the carbon amount of the 18.5-CoS/C is approximately 7.4 wt% detected by the CHNSO test, which is not sufficient to coat the numerous CoS nanoparticles, resulting in the overflowing of nanoparticles on the higher calcination temperature (Fig. S2a,b). The specific carbonization and sulfidation process were explored by observing morphology of the products with different temperature and heat time as shown in Fig. S3. The precursor Co-MOF exhibits smooth surface. When temperature reaches 400 °C, the nanorod surface cracks and forms porous structure owing to the decomposition of organic ligand and the release of the gas. When temperature reaches 600 °C, some nanoparticles emerge on the surface of the framework. With heat time approaches 2 h, the surface is fully covered by CoS nanoparticles. Fig. 1i displays EDS colour mapping of the 7-CoS/C, which demonstrates that Co, S, and C components are homogeneously distributed in the nanorod frameworks.

Fig. 2a shows Raman spectrum of the 7-CoS/C, and the peak at 659 cm⁻¹ is assigned to A_{1g} mode of CoS [26]. Two strong peaks are located at around 1566 and 1334 cm⁻¹ which correspond to G band of graphitic carbon (E_{2g} mode) and D band of disordered carbon (A_{1g} mode), respectively [38]. The intensity ratio of the D band to G band (I_D/I_G) is 1.04, indicating high graphitization degree of the carbon nanorods. The G band and D band can be fitted into four peaks. The peaks at around 1566 and 1334 cm⁻¹ are assigned to sp²-type carbon vibrations, while the other two peaks at about 1470 and 1182 cm⁻¹ are related to sp³-type carbon vibrations [38]. The A_{sp3}/A_{sp2} of the 7-CoS/C is 0.27, revealing that highly conductive sp²-type carbon is obviously dominant. Fig. 2b exhibits N₂ adsorption/desorption isotherm of the 7-CoS/C, and the curves are indexed to type IV isotherm according to the IUPAC classification, suggesting a pore size in a mesopore range. The BET specific surface area and total pore volume are 387.6 m² g⁻¹ and 0.457 cm³ g⁻¹, respectively. The large surface area and pore volume enable to effectively provide a large interface to facilitate electrochemical uptake and release of Na⁺ during the cycles. The inset in Fig. 2b presents that the 7-CoS/C has narrow pore distribution with an average pore size of 5 nm. N₂ adsorption/desorption isotherm of the 18.5-CoS/C is shown in Fig. S4, and its BET specific surface area and total pore volume are only 149.7 m² g⁻¹ and 0.243 cm³ g⁻¹, respectively. Fig. 2c-f depict XPS data of the 7-CoS/C. There are six peaks in the fitted Co spectra (Fig. 2c): Co 2p_{3/2} of CoS at 778.3 and 780.9 eV and satellite peak at 785 eV as well as 2p_{1/2} of CoS at 793.7 and 797.5 eV and satellite peak at 803.1 eV [26]. High resolution S 2p spectrum in Fig. 2d displays four fitted peaks, which not only shows S peak of CoS at 161.7 and 162.8 eV but also demonstrates the doping of S in carbon nanorods (164.8 eV) and the interaction between CoS and carbon nanorods (163.8 eV) [39]. The C 1s spectrum in Fig. 2e confirms the existence of C-N bond (288.6 eV) and graphitic carbon (285.6 eV) [40]. High resolution N 1s spectrum in Fig. 2e reveals that the existence forms of N are pyridinic and graphitic N (Fig. 2g) [39]. The area percentages of pyridinic and graphitic N are 34.8% and 65.2%,

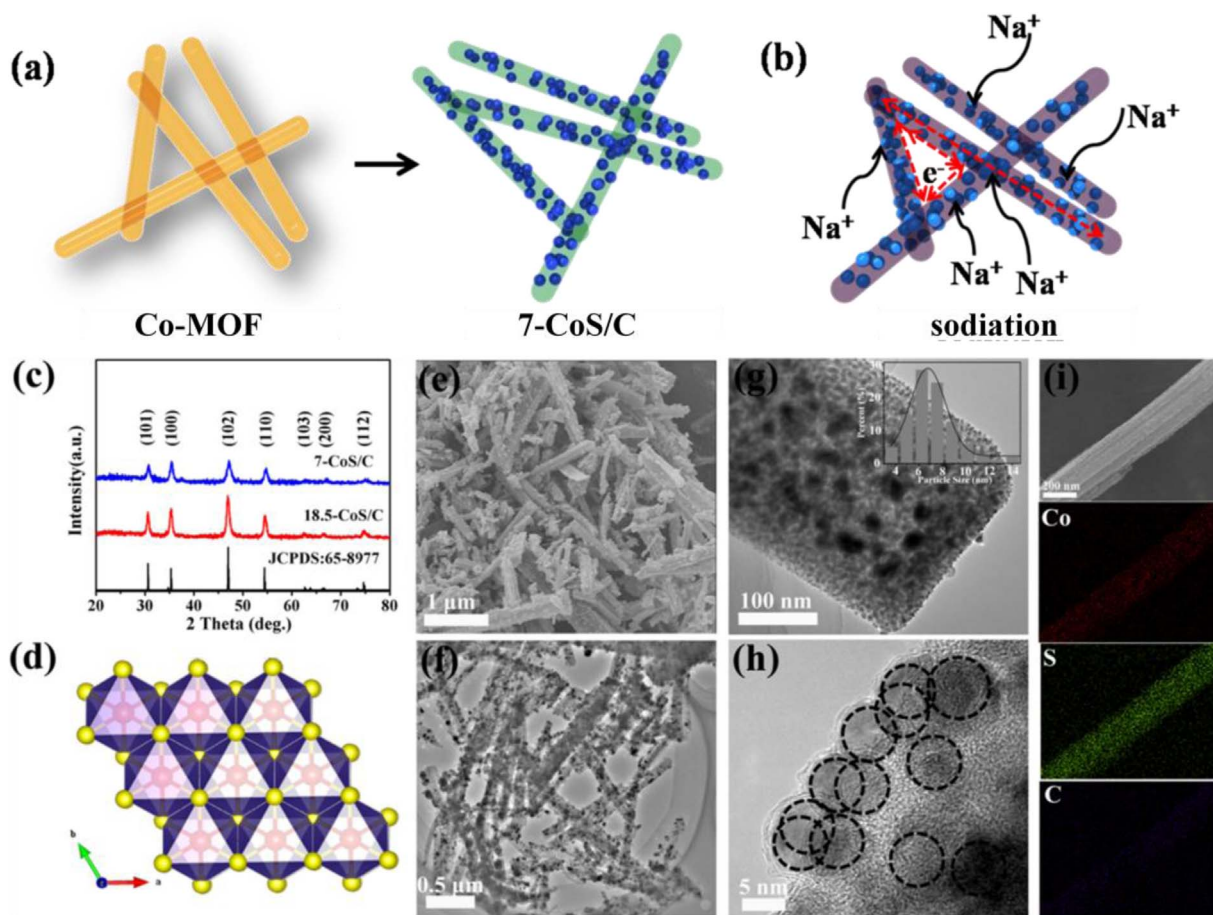


Fig. 1. Brief illustration of the synthesis process (a) and sodium-storage process (b) of the 7-CoS/C. Phase analysis: (c) XRD pattern of the as-prepared 7-CoS/C and 18.5-CoS/C; (d) crystal structure of hexagonal CoS. Morphology characterization: SEM (e), TEM (f,g), (inset: CoS particle size distribution diagram), high-resolution TEM (HRTEM) (h), and EDS mapping (Co, S, C elements) (i) of the as-prepared 7-CoS/C.

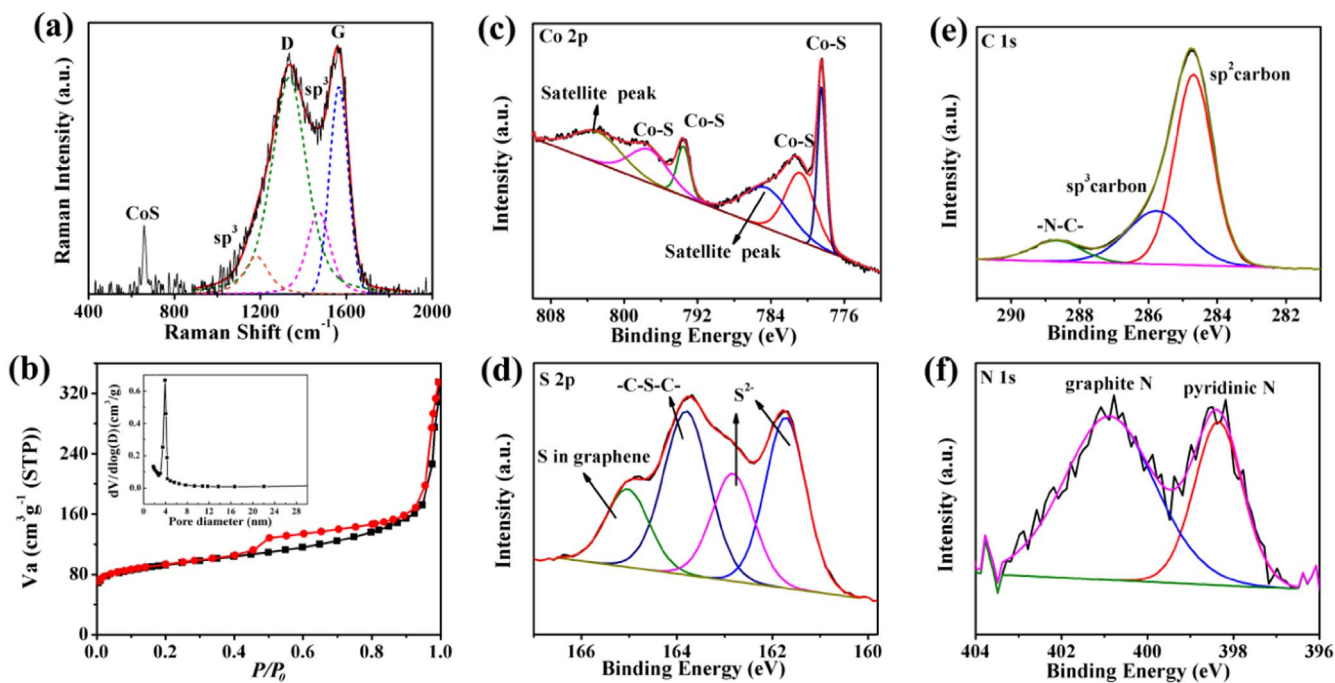


Fig. 2. Phase analysis: (a) Raman spectrum, (b) N_2 adsorption–desorption isotherm and pore size distribution curve (inset) of the as-prepared 7-CoS/C. (c) High-resolution Co 2p, (d) S 2p, (e) C 1s, and (f) N 1s XPS spectra of the 7-CoS/C.

respectively. Beneficially, the N-doping can enrich the conjugated electrons, facilitating the enhancement of electronic conductivity and create some defects in carbon nanorods, providing more active sites for Na^+ insertion [41].

Motivated by porous carbon frameworks decorated with ultrafine CoS nanoparticles, electrochemical properties of the as-prepared 7-CoS/C were tested by assembling 7-CoS/C-Na half cells. The working electrode with a diameter of 6 mm disk was prepared by direct compression without the utilization of current collector. And the mass of each disk is 1.8 mg, by which we can calculate the cathode loading amount is 6.37 mg cm^{-2} . The liquid electrolyte and operating voltage range were optimized first. For electrolytes, discharge capacities rapidly attenuate when using carbonate-based electrolytes (Fig. S5c, d). The discharge capacities with 1 M NaSO_3CF_3 and NaClO_4 in DGM are 538 mAh g^{-1} after 50 cycles and 492 mAh g^{-1} after 30 cycles at 1 A g^{-1} , respectively, which correspond to capacity retention of 97.1% and 84.9% calculated from 1st cycle (Fig. S5a, b). In order to investigate the difference of the four electrolytes, the apparent activation energies (E_a) of electrochemical reactions with $\text{NaSO}_3\text{CF}_3/\text{DGM}$, $\text{NaClO}_4/\text{DGM}$, $\text{NaClO}_4/\text{EC-DMC}$, and NaClO_4/PC were analyzed from the EIS data and the Arrhenius plots as shown in Fig. S6, S7. The E_a of $\text{NaSO}_3\text{CF}_3/\text{DGM}$, $\text{NaClO}_4/\text{DGM}$, $\text{NaClO}_4/\text{EC-DMC}$, and NaClO_4/PC are 26.47, 41.47, 45.05, and $55.73 \text{ kJ mol}^{-1}$, respectively, indicating that the $\text{NaSO}_3\text{CF}_3/\text{DGM}$ electrolyte possesses best kinetics among the selected four electrolytes. It can be viewed that the difference in voltage profiles between the first cycle and the subsequent cycles, similar to the previous literature reported during the sodiation/desodiation process [25,26,33,42]. This behavior of deviation could be attributed to the charge/discharge reaction is controlled by kinetics and the overpotential requires to initiate and pursue the decomposition reaction [42]. With regards to voltage window, the capacity also seriously decays when cycling between 0.01 and 3 V (Fig. S8a). The cycling performance between 0.01 and 3 V (Fig. S8b) presents that the specific capacity sharply declines from 871 to about 200 mAh g^{-1} at 0.5 A g^{-1} at the first 40 cycles. It may result from irreversible reaction and larger structure change caused by deep discharge, which lead to the inactivation and

falling off of the active materials [26].

Fig. 3a–b compare cycling and rate performance of the 7-CoS/C and 18.5-CoS/C samples. After 2000 cycles at 1 A g^{-1} , the 7-CoS/C still remains a high capacity of 542 mAh g^{-1} , but the capacity of the 18.5-CoS/C is only 314 mAh g^{-1} (Fig. 3a). What's more, the 18.5-CoS/C rapidly declines during the initial 300 cycles. Nanoparticles can partially absorb volume change during the charge-discharge processes [25], promoting the integrity of the electrode. The 7-CoS/C has smaller particle size than that of the 18.5-CoS/C, leading to higher capacity and better cycling stability. Fig. 3b shows rate capabilities of the 7-CoS/C and 18.5-CoS/C samples. The 7-CoS/C sample shows discharge capacities of 596, 584, 552, 538, 510, 458, 400, and 362 mAh g^{-1} at 0.2, 0.5, 1, 2, 5, 10, 20, 40 A g^{-1} , respectively. However, the 18.5-CoS/C delivers lower capacities at each current density than those of the 7-CoS/C. At 40 A g^{-1} , its capacity is only 214 mAh g^{-1} . According to previous reports [43–46], the diffusion time is related to diffusion length and Na^+ diffusion coefficient as follows:

$$\tau = L_{\text{ion}}^2 / D_{\text{Na}}$$

Thus, downsizing the particle size can shorten the Na^+ diffusion length, leading to high-rate capability of active materials. Besides, we can see that the discrepancy between the two samples at 10 A g^{-1} is larger than the discrepancy at 40 A g^{-1} , which is similar to the phenomenon of reported literature [47]. The utilization of active materials is maximized at the low current density, reflected by the less obvious capacity difference. As the current density increases, electrochemical reaction controlled by ionic diffusion gradually decreased and the percentage of pseudocapacitive behavior becomes greater, which has been presented in our following reaction kinetic investigation. When the current density reaches 10 A g^{-1} , ionic diffusion behavior is supposed to almost disappear, giving rise to the largest capacity discrepancy. Fig. 3c, d present linear fit of the average voltage vs. the square root of the current intensity of the 7-CoS/C and 18.5-CoS/C samples. The 7-CoS/C exhibits less ΔV at each current density and smaller absolute value of slope than those of the 18.5-CoS/C, indicating slighter polarization of the 7-CoS/C electrode material. The relative

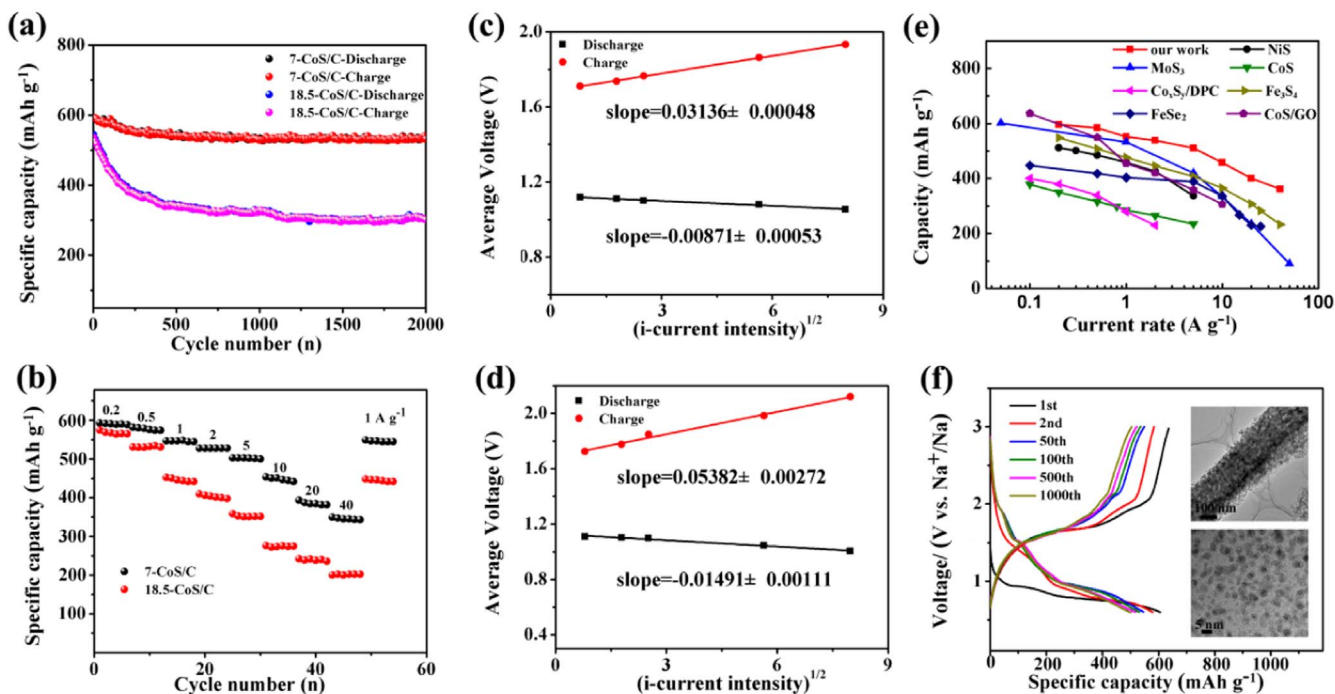


Fig. 3. (a) Cycling performance at a current density of 1 A g^{-1} in the voltage range of 0.6–3 V vs Na^+/Na and (b) rate capability of the 7-CoS/C and 18.5-CoS/C electrodes. Linear fit of the average voltage vs. the square root of the current intensity of (c) 7-CoS/C and (d) 18.5-CoS/C electrode. (e) Comparison with other typical anode materials of NIBs. (f) Galvanostatic discharge/charge profiles tested at a current density of 5 A g^{-1} of the 7-CoS/C electrode in the voltage range of 0.6–3 V vs Na^+/Na , (inset: TEM and HRTEM of the 7-CoS/C after 200 cycles).

data has been clearly presented in Table S1. As Table S1 shown, the difference between charge and discharge average voltage of the 7-CoS/C is relatively lower compared with that of 18.5-CoS/C. The electrochemical impedance spectra (EIS) of different-sized CoS nanocomposite are compared in Fig. S9. It can be seen that the 7-CoS/C exhibits relatively low charge-transfer resistance than that of the 18.5-CoS/C on both original state and the charge state after 50 cycles. The fast charge-transfer kinetics of the 7-CoS/C is attributed to the design of smaller CoS grains and porous carbon matrix, which is favorable for decreasing the diffusion obstacle of Na^+ , enhancing the electronic conductivity, and providing more transport channel for Na^+ insertion/extraction. The excellent rate performance of the 7-CoS/C is compared with other anode materials (Fig. 3e) [12,14,26,33,48–50] the as-prepared 7-CoS/C reveals obvious advantages at more than 1 A g^{-1} . Fig. 3f shows the charge-discharge curves of the 7-CoS/C at 5 A g^{-1} , delivering a discharge capacity of 504 mAh g^{-1} after 1000 cycles. Considering the solubility of polysulfide, the amount of dissolved sulfur in the organic electrolyte was determined. The comparison of sulfur amount on the electrode before and after 100 cycles was adopted. The sulfur content of fresh electrode is approximately 24.3 wt% detected by ICP test. On cycling for 100 cycles, the cell was dismantled and the electrode was washed with DGM solvent before vacuum drying. Then the sulfur amount of the cycled electrode was tested to be 23.2 wt%. The negligible discrepancy reveals the excellent retention sulfur effect of the 7-CoS/C structure in the charge/discharge process. Specifically, in situ generated thin carbon layers and embedded architecture are simultaneously conducive to confine sulfide for relieving the loss of active materials and enhancing the rate capability and cycling stability of the 7-CoS/C. Also, the choice of ether-based electrolyte would probably restrain the side reaction between polysulfides and electrolyte [26]. Besides, the TEM and HRTEM images of the 7-CoS/C after 200 cycles revealed in the inset of Fig. 3f indicate that the design of embedded porous structure enables to preserve the pristine structure and morphology with each CoS grains homogeneously confined in the porous carbon nanorods. The result proves that the tailored architecture effectively restrains the agglomeration and pulverization of active materials during the repeated sodiation/desodiation process, thus contributing to the long cycle life and the material utilization. However, the 18.5-CoS/C failed to stand the mechanical stress, bringing about the agglomeration of nanoparticles (Fig. S10) due to falling off from the carbon nanorods, which is responsible for the rapidly decreasing capacity. It demonstrates that embedded porous construct and the coverage of thin carbon layer play key role in simultaneously immobilizing and protecting active materials.

To further study the reaction kinetic of the 7-CoS/C, CV test at different scan rates were carried on. As shown in Fig. 4a, all peak currents (i) upgrade as the scan rates (v) ascend. Fig. 4b presents $\log(i)$ vs. $\log(v)$ plots of the five redox peaks, and the slope of the fitted line is represented by b . When $b=0.5$, the electrochemical reaction is controlled by ionic diffusion, and when $b=1$, pseudocapacitive behaviors are dominant [48,51]. The calculated b -values are 0.68, 0.93, 0.72, 0.88, and 1.05. Fig. 4c lists pseudocapacitive contributions at various scan rates. The contribution percents are 72.9%, 76.1%, 78.2%, 81.1%, and 83.0% at the scan rates of 0.1, 0.3, 0.5, 0.8, and 1.0 mV s^{-1} , respectively, revealing that the pseudocapacitive Na-storage amount occupies a high percent of the whole capacity. Fig. 4d exhibits the special pseudocapacitive fraction at 0.8 mV s^{-1} , which is analogy to the behavior of metal oxides and metal chalcogenides [51–53]. As a result, high-rate capability is achieved on embedded porous 7-CoS/C.

Fig. 5a shows the near-edge X-ray absorption spectra (XANES) of the 7-CoS/C electrode at different charged/discharged states. Notably, when discharging to 1.4 and 0.6 V, the Co K-edge position slightly shifted to the position of Co power due to the appearance of conversion reaction. In contrast, the Co K-edge position changed toward the opposite direction at charged 1.7 and 3.0 V. However, the concave and convex positions of all charged/discharged states are in coordination

with the pristine CoS, indicating that there is slight structure change of charge/discharge products favorable for the excellent cycle performance. Fig. 5b, c exhibit XPS curves of the Co collected at fully discharged and charged states. When discharged to 0.6 V, the fitted peaks of Co $2p_{3/2}$ are ascribed to Co (0) and surface-adsorbed hydroxide species. When charged to 3 V, Co turns into Co^{2+} , illustrating the good cycle reversibility during repeated sodiation/desodiation process. What's more, *ex situ* XRD patterns of the 7-CoS/C on different charge/discharge states after 200 cycles were displayed in Fig. S11. When fully discharged to 0.6 V, the peaks at 23° , 38° , 44° , and 51° can be ascribed to (111), (220) crystal planes of Na_2S and (111), (200) crystal planes of Co, respectively. Upon fully charged state, CoS could be reversibly emerged, which is associated with the cycling stability of the 7-CoS/C electrode with embedded construct and uniform nanograins. At fully discharged state (0.6 V) of the CoS electrodes, the diffraction rings of (200) planes of Co emerge in the SAED pattern (Fig. 5d), although their definition is poor due to the low-crystalline Co structure. Fig. 5e presents the SAED pattern at fully charged state, in which the diffraction dots of (110), (102), and (203) plane of CoS are found.

Along with the superb electrochemical properties of the 7-CoS/C-Na half-cell, the exploration of full cell has been investigated. $\text{Na}_3\text{V}_2(\text{PO}_4)_3$ with a NASICON structure was attempted to utilize as cathode material for the full cell, owing to the excellent work voltage and slight polarization during Na^+ intercalation/deintercalation [54]. The full battery was assembled based on the capacity ratio of 1-1.2:1 between the $\text{Na}_3\text{V}_2(\text{PO}_4)_3$ cathode and 7-CoS/C anode, by which we could ensure the maximized material utilization and reasonably evaluate the electrochemical property of the 7-CoS/C. Fig. 6a shows charge-discharge curves of the $\text{Na}_3\text{V}_2(\text{PO}_4)_3/7\text{-CoS/C}$ full cell with excessive $\text{Na}_3\text{V}_2(\text{PO}_4)_3$ at 0.5 A g^{-1} . The full cell delivers a discharge capacity of 368 mAh g^{-1} in the 2nd cycle based on the mass of 7-CoS/C. After 100 cycles, the discharge capacity maintains 352 mAh g^{-1} (Fig. 6b), corresponding to a capacity retention of 95.6% calculated from the 2nd cycle. The coulombic efficiencies from the 2nd cycle to the 100th cycle are approximately 100%. The excellent performance of both 7-CoS/C-Na battery and $\text{Na}_3\text{V}_2(\text{PO}_4)_3/7\text{-CoS/C}$ full cell demonstrates that the 7-CoS/C is an extremely promising anode materials for potential applications.

The excellent rate capability and superior cycling stability of the 7-CoS/C can be ascribed to the synergistic effect stemmed from the extreme nano-hybridization. First, the thin graphitic carbon layer enables to not only enhance electronic conductivity, but also serve as a support matrix to mitigate mechanical strain and decrease interface impedance among nanoparticles [23]. Second, the ultrafine grains with $\sim 7 \text{ nm}$ significantly shorten the diffusion distance, contributing to the rate of insertion/extraction as reflected by the superior rate performance and large proportion of pseudocapacitive Na-storage performance. Third, porous one-dimensional features can accommodate the volume variation during the repeated sodiation/desodiation process and afford more transport channel to allow the electrolyte easily penetrate frameworks [27,28,45]. More importantly, embedded nano-structure derived from in-situ carbonization and sulfidation renders the reinforcement of coupling force [23], suppressing the entire electrode agglomeration and stripping and structural degradation [27] proved by the after-cycling morphology, which further promotes remarkable electrochemical performance by maximizing utilization and stabilizing the structure of electrode materials.

3. Conclusion

In conclusion, ultrafine CoS nanoparticles ($\sim 7 \text{ nm}$) embedded in porous carbon nanorods have been successfully synthesized by a facile heating treatment of Co-MOF in an atmosphere of sulfide sublimation. Significantly, the unique architectures enable to realize the capacity of 542 mAh g^{-1} after 2000 cycles at 1 A g^{-1} and excellent rate perfor-

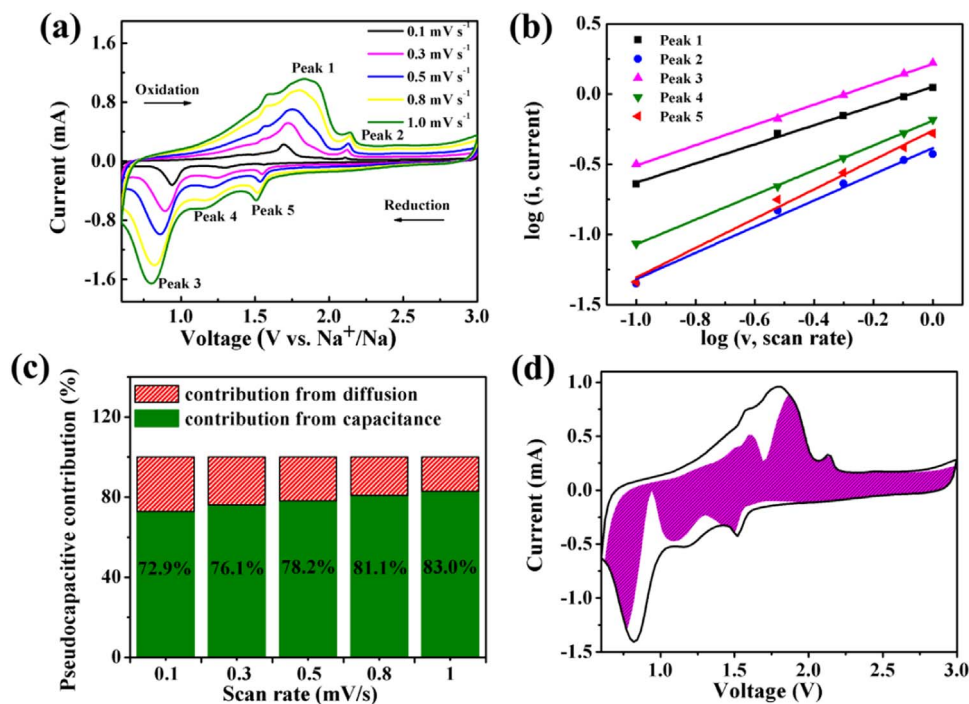


Fig. 4. Kinetics investigation: CV curves at different scan rates after 200 cycles (a), corresponding $\log i$ vs. $\log v$ plots at different redox states of the as-prepared 7-CoS/C electrode (b), bar chart showing the percent of pseudocapacitive contribution at different scan rates (c); CV curve with the pseudocapacitive fraction shown by the magenta region at a scan rate of 0.8 mV s^{-1} (d).

mance. Even at an ultrahigh current density of 40 A g^{-1} , the discharge capacity still reaches 356 mAh g^{-1} . The nano-sized embedded porous structure is proved to be favorable for decreasing polarization effect and preserving pristine immobile sites of active CoS materials. In addition, discharge capacity of 368 mAh g^{-1} in the 2nd cycle of $\text{Na}_3\text{V}_2(\text{PO}_4)_3/7\text{-CoS/C}$ full cell will also spur the development of novel embedded nano-architecture design. This MOF-driven approach can be generally extended to other porous embedded hybridization with great potential for future energy-storage materials.

4. Experimental section

4.1. Sample synthesis

7-CoS/C and 18.5-CoS/C were prepared by one-step heating treatment of Co-MOF and sublimed sulfur. For Co-MOF, 3 mmol $\text{Co}(\text{NO}_3)_2 \cdot 6\text{H}_2\text{O}$ (0.876g), 3 mmol 1,3,5-benzenetricarboxylic acid (H_3BTC) (0.633g), and 3 mmol 4,4'-bipyridine (4,4'-bipy) (0.576g) as starting materials were dissolved into 60 mL of dimethylformamide

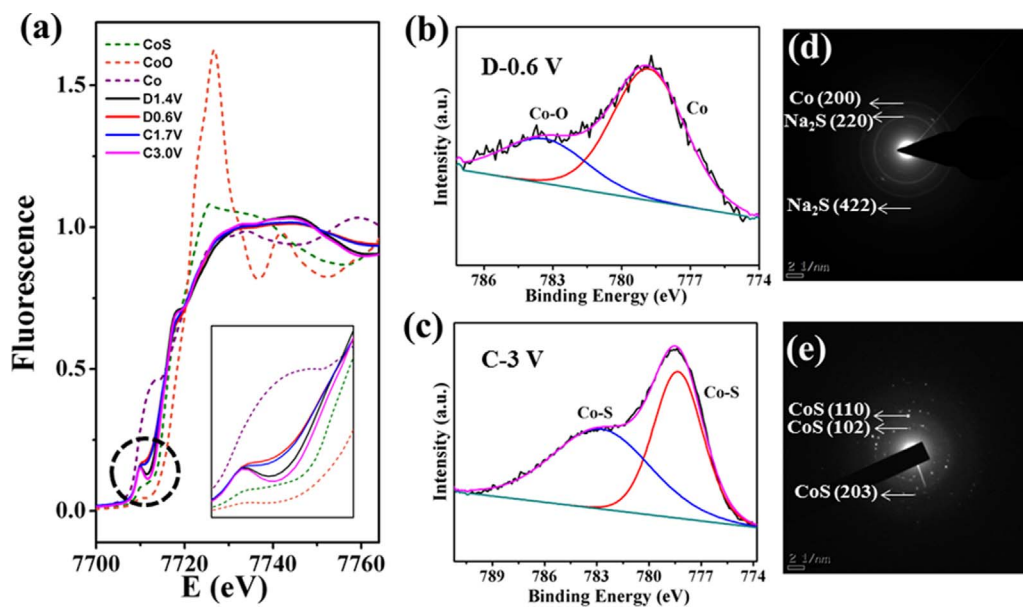


Fig. 5. Reaction mechanism: Near-edge X-ray absorption spectroscopy of the 7-CoS/C electrodes at different cycling states and the reference Co, CoO, and CoS (a), as well as the magnification of the region between 7708 and 7715 eV (inset), XPS curves of the Co 2p (b, c) orbitals collected at fully discharged and charged states (b. discharged 0.6 V, c. charged 3.0 V), SAED patterns of the 7-CoS/C electrodes at fully discharged (0.6 V) (d) and charged (3 V) (e) states.

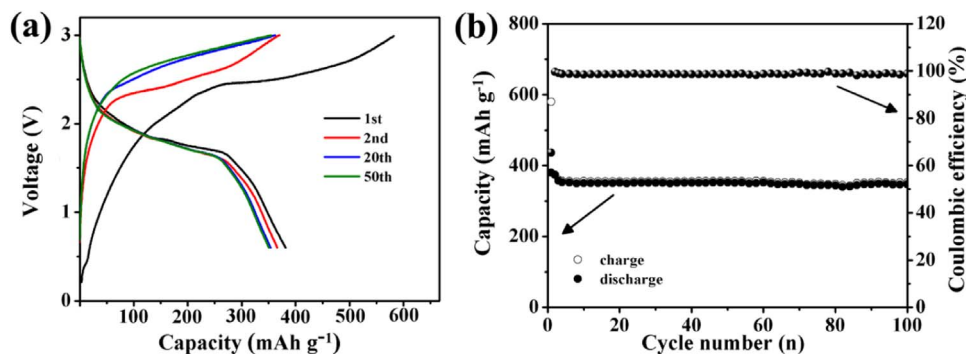


Fig. 6. Charge and discharge curves at different cycles (a) and cycling performance (b) of the $\text{Na}_3\text{V}_2(\text{PO}_4)_3/7\text{-CoS/C}$ full cell with excessive $\text{Na}_3\text{V}_2(\text{PO}_4)_3$ at 0.5 A g^{-1} .

(DMF). After vigorous stirring for 30 min, the purple solution was transferred into a Teflon-lined stainless-steel autoclave with sealing and heated at $120 \text{ }^\circ\text{C}$ for 4 h. The as-obtained product was centrifuged and washed thoroughly with DMF and absolute ethanol. The pink powder was dried at $80 \text{ }^\circ\text{C}$ for 12 h under vacuum. Then, the mixture of Co-MOF and sublimed sulfur was directly calcinated at $600 \text{ }^\circ\text{C}$ for 2 h to obtain the 7-CoS/C under vacuum atmosphere. For comparison, similar process was operated and only replaced the calcination temperature with $800 \text{ }^\circ\text{C}$ to obtain the 18.5-CoS/C.

4.2. Structure characterization

The structure of the as-prepared samples was characterized by a D8 Advance X-ray diffractometer, (XRD, Cu $K\alpha$ radiation, $\lambda=1.5418 \text{ \AA}$) and Raman spectra (Renishaw INVIA micro-Raman spectroscopy system). The morphology and microstructure of the 7-CoS/C and 18.5-CoS/C were analyzed by a field-emission scanning electron microscopy (FESEM, JEOL, JSM-7100F) and a transmission electron microscopy (TEM, JEOL, JEM-2100F). The chemical states of elements were evaluated by X-ray photoelectron spectroscopy (XPS, VG MultiLab 2000). Brunauer-Emmett-Teller surface area was measured using Tristar II 3020 instrument by adsorption of nitrogen at 77 K . TG analysis was performed using NETZSCH-STA449c/3/G thermoanalyzer. Co K-edge X-ray adsorption near the edge structure (XANES) was performed in 10C beam line at Pohang Accelerating Laboratory (PAL) in Republic of Korea using a double Si (111) monochromator. The composition and the thickness of the cell electrodes allowed transmission mode measurements. All spectra were normalized to the main edge jump.

4.3. Electrochemical measurements

The electrochemical measurements were carried out with CR2032 coin-type half cells. The working electrode was made by cutting homogeneous mixture composed of the as-prepared active materials, acetylene black (AB), poly(tetrafluoroethylene) (PTFE) with a mass ratio of 8: 1: 1 into 6 mm disk. Glass fiber filter paper was used as a separator. Metallic Na film was used as both reference and counter electrodes. The coin cells were assembled in an argon-filled glove box. Galvanostatic tests were performed between 0.6 and 3 V with a multichannel battery testing system (LAND CT2001A). Cyclic voltammetry (CV) and electrochemical impedance spectrum (EIS) measurements were collected by an Autolab electrochemical workstation.

Acknowledgements

This work was supported by the National Key Research and Development Program of China (2016YFA0202603), the National Basic Research Program of China (2013CB934103), the Program of Introducing Talents of Discipline to Universities (B17034), the

National Natural Science Foundation of China (51521001, 51602239), the National Natural Science Fund for Distinguished Young Scholars (51425204), the Hubei Provincial Natural Science Foundation of China (2016CFB267), and the Fundamental Research Funds for the Central Universities (WUT: 2016III001, 2016III003, 2016IVA090, 2017III009, 2017III007), China postdoctoral Science Foundation (2016M592401). Prof. Liqiang Mai gratefully acknowledged financial support from China Scholarship Council (No. 201606955096). K. Zhang would like to acknowledge Korea Research Fellowship Program through the National Research Foundation of Korea (NRF) funded by the Ministry of Science, ICT and Future Planning (No. 2016H1D3A1906790).

Appendix A. Supporting information

Supplementary data associated with this article can be found in the online version at doi:10.1016/j.nanoen.2017.03.052.

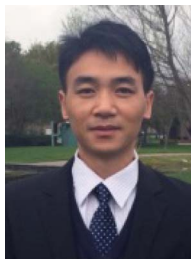
References

- [1] B. Dunn, H. Kamath, J.M. Tarascon, *Science* 334 (2011) 928–935.
- [2] M.V. Reddy, G.V. Subba Rao, B.V.R. Chowdari, *Chem. Rev.* 113 (2013) 5364–5457.
- [3] N. Yabuuchi, K. Kubota, M. Dahbi, S. Komaba, *Chem. Rev.* 114 (2014) 11636–11682.
- [4] Y. Yu, L. Gu, C. Zhu, P.A. van Aken, J. Maier, *J. Am. Chem. Soc.* 131 (2009) 15984–15985.
- [5] M.D. Slater, D. Kim, E. Lee, C.S. Johnson, *Adv. Funct. Mater.* 23 (2013) 947–958.
- [6] D. Kundu, E. Talaie, V. Duffort, L.F. Nazar, *Angew. Chem. Int. Ed.* 54 (2015) 3431–3448.
- [7] B.L. Ellis, L.F. Nazar, *Curr. Opin. Solid State Mater. Sci.* 16 (2012) 168–177.
- [8] Z.H. Nie, D. Fava, E. Kumacheva, S. Zou, G.C. Walker, M. Rubinstein, *Nat. Mater.* 6 (2007) 609–614.
- [9] V.L. Chevrier, G. Ceder, *J. Electrochem. Soc.* 158 (2011) A1011–A1014.
- [10] H.L. Pan, Y.S. Hu, L.Q. Chen, *Energy Environ. Sci.* 6 (2013) 2338–2360.
- [11] P. Sengutturan, G. Rousse, M.E. Arroyo de Dompablo, H. Vezin, J.M. Tarascon, M.R. Palacin, *J. Am. Chem. Soc.* 135 (2013) 3897–3903.
- [12] D. Zhang, W. Sun, Y. Zhang, Y. Dou, Y. Jiang, S.X. Dou, *Adv. Funct. Mater.* 26 (2016) 7479–7485.
- [13] Y.X. Wang, J. Yang, S.L. Chou, H.K. Liu, W.X. Zhang, D. Zhao, S.X. Dou, *Nat. Commun.* 6 (2015) 8689.
- [14] K. Wu, Y. Jiang, P. Kopold, P.A. van Aken, J. Maier, Y. Yu, *Adv. Mater.* 28 (2016) 7276–7283.
- [15] Y. Li, Y. Liang, F.C. Robles Hernandez, H. Deog Yoo, Q. An, Y. Yao, *Nano Energy* 15 (2015) 453–461.
- [16] Y. Zhou, D. Yan, H. Xu, J. Feng, X. Jiang, J. Yue, J. Yang, Y. Qian, *Nano Energy* 12 (2015) 528–537.
- [17] M. Zanini, J. Shaw, G. Tennenhouse, *J. Electrochem. Soc.* 128 (1981) 1647–1650.
- [18] C. Xu, Y. Xu, C. Tang, Q. Wei, J. Meng, L. Huang, L. Zhou, G. Zhang, L. He, L. Mai, *Nano Energy* 28 (2016) 224–231.
- [19] K. Saravanan, C.W. Mason, A. Rudola, K.H. Wong, P. Balaya, *Adv. Energy Mater.* 3 (2013) 444–450.
- [20] C. Delmas, A. Nadiri, J. Soubeyroux, *Solid State Ion.* 28 (1988) 419–423.
- [21] H. Kim, J. Hong, Y.-U. Park, J. Kim, I. Hwang, K. Kang, *Adv. Funct. Mater.* 25 (2015) 534–541.
- [22] Y. Gu, Y. Xu, Y. Wang, *ACS Appl. Mater. Interfaces* 5 (2013) 801–806.
- [23] R. Wu, D.P. Wang, X. Rui, B. Liu, K. Zhou, A.W. Law, Q. Yan, J. Wei, Z. Chen, *Adv. Mater.* 27 (2015) 3038–3044.
- [24] Z. Hu, L. Wang, K. Zhang, J. Wang, F. Cheng, Z. Tao, J. Chen, *Angew. Chem. Int. Ed.* 126 (2014) 13008–13012.

- [25] Q. Zhou, L. Liu, G. Guo, Z. Yan, J. Tan, Z. Huang, X. Chen, X. Wang, *RSC Adv.* 5 (2015) 71644–71651.
- [26] S. Peng, X. Han, L. Li, Z. Zhu, F. Cheng, M. Srinivansan, S. Adams, S. Ramakrishna, *Small* 12 (2016) 1359–1368.
- [27] Z. Zhu, S. Wang, J. Du, Q. Jin, T. Zhang, F. Cheng, J. Chen, *Nano Lett.* 14 (2014) 153–157.
- [28] Y. Liu, N. Zhang, L. Jiao, J. Chen, *Adv. Mater.* 27 (2015) 6702–6707.
- [29] Y. Liu, N. Zhang, L. Jiao, Z. Tao, J. Chen, *Adv. Funct. Mater.* 25 (2015) 214–220.
- [30] C. Niu, J. Meng, X. Wang, C. Han, M. Yan, K. Zhao, X. Xu, W. Ren, Y. Zhao, L. Xu, Q. Zhang, D. Zhao, L. Mai, *Nat. Commun.* 6 (2015) 7402.
- [31] N. Zhang, X. Han, Y. Liu, X. Hu, Q. Zhao, J. Chen, *Adv. Energy Mater.* 5 (2015) 1401123.
- [32] Y. Liu, N. Zhang, C. Yu, L. Jiao, J. Chen, *Nano Lett.* 16 (2016) 3321–3328.
- [33] Z. Zhang, Y. Gan, Y. Lai, X. Shi, W. Chen, J. Li, *RSC Adv.* 5 (2015) 103410–103413.
- [34] K. Zhang, M. Park, L. Zhou, G.H. Lee, J. Shin, Z. Hu, S.L. Chou, J. Chen, Y.M. Kang, *Angew. Chem. Int. Ed.* 55 (2016) 12822–12826.
- [35] D. Gu, W. Li, F. Wang, H. Bongard, B. Spliethoff, W. Schmidt, C. Weidenthaler, Y. Xia, D. Zhao, F. Schüth, *Angew. Chem. Int. Ed.* 54 (2015) 7060–7064.
- [36] W. Li, F. Wang, Y. Liu, J. Wang, J. Yang, L. Zhang, A.A. Elzatahry, D. Al-Dahyan, Y. Xia, D. Zhao, *Nano Lett.* 15 (2015) 2186–2193.
- [37] L. Zhou, T. Zhang, Z. Tao, J. Chen, *Nano Res.* 7 (2014) 774–781.
- [38] Z. Zhu, F. Cheng, J. Chen, *J. Mater. Chem. A* 1 (2013) 9484–9490.
- [39] P. Ganesan, M. Prabu, J. Sanetuntikul, S. Shanmugam, *ACS Catal.* 5 (2015) 3625–3637.
- [40] P. Zhang, F. Sun, Z. Xiang, Z. Shen, J. Yun, D. Cao, *Energy Environ. Sci.* 7 (2014) 442–450.
- [41] W. Shen, C. Wang, Q. Xu, H. Liu, Y. Wang, *Adv. Energy Mater.* 5 (2015) 1400982.
- [42] J.M. Yan, H.Z. Huang, J. Zhang, Z.J. Liu, Y. Yang, *J. Power Sources* 146 (2005) 264–269.
- [43] A.S. Arico, P. Bruce, B. Scrosati, J.-M. Tarascon, W. Van Schalkwijk, *Nat. Mater.* 4 (2005) 366–377.
- [44] P.G. Bruce, B. Scrosati, J.M. Tarascon, *Angew. Chem. Int. Ed.* 47 (2008) 2930–2946.
- [45] J.B. Goodenough, K.-S. Park, *J. Am. Chem. Soc.* 135 (2013) 1167–1176.
- [46] Q. Wei, Q. An, D. Chen, L. Mai, S. Chen, Y. Zhao, K.M. Hercule, L. Xu, A. Minhas-Khan, Q. Zhang, *Nano Lett.* 14 (2014) 1042–1048.
- [47] S. Yuan, Y.-H. Zhu, W. Li, S. Wang, D. Xu, L. Li, Y. Zhang, X.-B. Zhang, *Adv. Mater.* 29 (2017). <http://dx.doi.org/10.1002/adma.201602469>.
- [48] K. Zhang, Z. Hu, X. Liu, Z. Tao, J. Chen, *Adv. Mater.* 27 (2015) 3305–3309.
- [49] H. Ye, L. Wang, S. Deng, X. Zeng, K. Nie, P.N. Duchesne, B. Wang, S. Liu, J. Zhou, F. Zhao, N. Han, P. Zhang, J. Zhong, X. Sun, Y. Li, Y. Li, J. Lu, *Adv. Energy Mater.* (2016) 1601602.
- [50] Q. Li, Q. Wei, W. Zuo, L. Huang, W. Luo, Q. An, V.O. Pelenovich, L. Mai, Q. Zhang, *Chem. Sci.* (2016). <http://dx.doi.org/10.1039/C6SC02716D>.
- [51] T. Brezesinski, J. Wang, S.H. Tolbert, B. Dunn, *Nat. Mater.* 9 (2010) 146–151.
- [52] Z. Hu, Z. Zhu, F. Cheng, K. Zhang, J. Wang, C. Chen, J. Chen, *Energy Environ. Sci.* 8 (2015) 1309–1316.
- [53] K. Zhang, M. Park, L. Zhou, G.H. Lee, W. Li, Y.M. Kang, J. Chen, *Adv. Funct. Mater.* 26 (2016) 6728–6735.
- [54] Y. Xu, Q. Wei, C. Xu, Q. Li, Q. An, P. Zhang, J. Sheng, L. Zhou, L. Mai, *Adv. Energy Mater.* 6 (2016) 1600389.



Jinzhi Sheng received his M.S. degree in Materials Engineering from Wuhan University of Technology in 2015. He is currently working toward the Ph.D. degree and his current research focuses on the energy storage materials and devices.



Qinyou An is Associate Professor of Materials Science and Engineering at Wuhan University of Technology (WUT). He received his Ph.D. degree from WUT in 2014. He carried out his postdoctoral research in the laboratory of Prof. Yan Yao at the University of Houston in 2014–2015. Currently, his research interest includes energy storage materials and devices.



Zhanliang Tao received his Ph.D. in Inorganic Chemistry from Nankai University in 2005. He has been an associated professor at the Key Laboratory of Advanced Energy Materials Chemistry (Ministry of Education) since 2008. His current research interests are focused on light weight nanomaterials for energy storage and conversion.



Yong-Mook Kang completed B.S. (1999), M.S. (2001), and Ph.D. (2004) at Korea Advanced Institute of Science and Technology. He has been a senior researcher at Samsung SDI Co., LTD. He is currently a professor in Department of Energy and Materials Engineering at Dongguk University-Seoul, as well as a TWAS (World Academy of Sciences for Developing Countries) young affiliate. His research area covers electrode or catalyst materials for Li rechargeable batteries and various post Li batteries, such as Li-O₂ battery, Na rechargeable battery, etc. In 2015, he has been appointed as RSC (Royal Society of Chemistry) fellow and representative in Korea.



Jun Chen is a Cheung Kong Scholar Professor, Director of Key Laboratory of Advanced Energy Materials Chemistry at Nankai University. He obtained his B.Sc. and M.Sc. degrees from Nankai University in 1989 and 1992, respectively, and his Ph.D. from Wollongong University (Australia) in 1999. He held the NEDO fellowship at National Institute of AIST Kansai Center (Japan) from 1999 to 2002. He has been working as a full professor on energy chemistry in Nankai University since 2002. His research activity focuses on nanostructured materials for electrochemical energy storage & conversion such as batteries, supercapacitors, fuel cells, and solar cells.



Limin Zhou received her M.S. degree from College of Chemistry at Nankai University in 2015. She is currently working toward the Ph.D. degree in Materials Engineering from Wuhan University of Technology. Her current research focuses on synthesis and characterization of advanced materials for sodium-ion batteries.



Kai Zhang received his Ph.D. in 2015 and B.S. in 2010 from College of Chemistry at Nankai University (China) under the supervision of Professor Jun Chen. Currently, he is a postdoctoral researcher in the group of Professor Yong-Mook Kang at the Department of Energy and Materials Engineering in Dongguk University-Seoul (Korea). His research focuses on lithium-ion, lithium-sulfur, and sodium-ion batteries



Liqiang Mai is Chair Professor of Materials Science and Engineering at Wuhan University of Technology (WUT). He received his Ph.D. from WUT in 2004. He carried out his postdoctoral research in the laboratory of Prof. Zhonglin Wang at Georgia Institute of Technology in 2006–2007 and worked as advanced research scholar in the laboratory of Prof. Charles M. Lieber at Harvard University in 2008–2011. He worked as advanced research scholar in the laboratory of Prof. Peidong Yang at University of California, Berkeley in 2017. His current research interests focus on nanowire materials and devices for energy storage. He received the National Natural Science Fund for Distinguished Young Scholars, the China Youth Science and Technology Award and so forth.